WEP Warwick Evans Publishing

International Journal of Mechanical and Electrical Engineering

ISSN: 3005-9615 (Print), ISSN: 3005-7132 (Online) | Volume 8, Number 5, Year 2026
DOI: https://doi.org/10.62051/ijmee.v8n5.04
Journal homepage: https://wepub.org/index.php/IJMEE/index

Beyond Hot Spots: Dual-Risk Thermal Instability in a 5 mm Asperity-Resolved Brake Contact Interface

Pengfei Cui [1, 2], Liangbi Wang [1, 2]

[1] School of Mechatronic Engineering, Lanzhou Jiaotong University, Lanzhou Gansu, 730070, China

[2] Key Laboratory of Railway Vehicle Thermal Engineering, Ministry of Education, Lanzhou Gansu, 730070, China

ABSTRACT

To reveal the differences in local thermal instability at rough braking interfaces under different load and rotational-speed conditions, a three-dimensional transient thermo-mechanically coupled finite element model was established. A 5×5×1 mm³ single-sided rough surface region containing 496 asperities was used as the computational domain. Temperature, stress, affected depth, energy dissipation, and frequency-domain fluctuations were compared under three operating conditions. The results show that, when the load increases from 12 kN to 16 kN, the maximum temperature rises from 957.03 °C to 993.10 °C, and the plastic-dissipation depth increases from 0.204 mm to 0.300 mm. Under a 16 kN load, reducing the rotational speed from 48 rad/s to 42 rad/s lowers the maximum temperature to 709.20 °C, but increases the root-mean-square stress amplitude to 265.79 MPa. Lowering the rotational speed can alleviate thermal concentration, but it cannot eliminate contact reconstruction and stress fluctuation induced by high load. Braking risk should therefore be evaluated jointly using the dual indicators of temperature concentration and stress fluctuation.

KEYWORDS

Rough Brake Contact Interface; Thermo-mechanical Coupling; Load-Speed Effect; Plastic Dissipation; Thermal Instability.

1. INTRODUCTION

High-speed train disc braking rapidly converts the mechanical energy of the vehicle into interfacial heat [6,9,10]. Because engineering surfaces consist of discrete asperities, the real load-bearing area is much smaller than the nominal contact area [1,3]. As a result, contact pressure and frictional power density concentrate around a small number of asperity peaks, giving rise to local flash temperature, thermal softening, subsurface plastic zones, and stress redistribution [1-3,10]. These local responses often occur before the macroscopic average temperature rise becomes evident, and they are important causes of hot spots, abnormal wear, and brake vibration [2,4,5,9].

Existing thermal analyses of braking systems usually use maximum temperature or average temperature rise as the primary evaluation quantity [4,5,9,10]. However, a decrease in temperature does not necessarily mean that the interface becomes more stable: when the normal load remains high, micro-contact spots may continue to engage, disengage, and reload, thereby intensifying stress fluctuations even at lower temperatures. It is therefore necessary to decouple the effects of load and rotational speed within the same rough computational domain, while simultaneously examining temperature concentration, plastic dissipation, and dynamic stress fluctuation.

In this study, a 5×5×1 mm³ single-sided rough region containing 496 asperities is selected as a statistically stable computational domain, and a transient thermo-mechanically coupled finite element model is established. Spatial fields, depth-wise affected layers, temporal responses, frequency-domain characteristics, and energy pathways are compared for three load-speed combinations. A dual-risk discrimination concept, distinguishing high-temperature-concentration risk from high-fluctuation risk, is then proposed to provide a multi-indicator basis for evaluating operating conditions at rough braking interfaces.

2. NUMERICAL MODEL AND EVALUATION METHOD

2.1. Contact Domain and Mesh

The computational model consists of a 50° sector brake disc and a 30° sector brake pad. The outer and inner radii of the brake disc are 370 mm and 220 mm, respectively, and the disc thickness is 20 mm. The outer radius, width, and thickness of the brake pad are 360 mm, 120 mm, and 14 mm, respectively. A 5×5×1 mm³ rough body is embedded at the center of the friction ring surface of the brake disc, while the remaining region is kept smooth. This configuration balances the resolution of local micro-contact with the structural and heat-conduction constraints of the overall model.

The rough topography is generated using the Weierstrass-Mandelbrot fractal function [7], with a fractal dimension of $D = 2.5$, a scale coefficient of $G = 3.0$, and a cutoff length of L_s=0.025 mm. The region contains 496 asperities, with an areal density of 19.84 asperities/mm² and an arithmetic mean roughness of R_a=0.06948 mm. After fixing the fractal parameters and random phases, the same topography is used for all three operating conditions, thereby preventing geometric randomness from masking the effects of load and rotational speed. The rough-surface expression is:

$$z(x,y) = L\left(\frac{G}{L}\right)^{D-2}\left(\frac{\ln\gamma}{M}\right)^{1/2} \sum_{m=1}^{M}\sum_{n=n_{\max}}^{n_{\max}} \gamma^{(D-3)n}\left\{\cos\phi_{m,n} - \cos\left[\frac{2\pi\gamma^n\sqrt{x^2+y^2}}{L}\cos\left(\tan^{-1}\left(\frac{y}{x}\right)-\frac{\pi m}{M}\right)+\phi_{m,n}\right]\right\} \tag{1}$$

where M is the number of superposed corrugations, $\varphi_{m,n}$ is the random phase, and γ is the frequency-scale parameter.

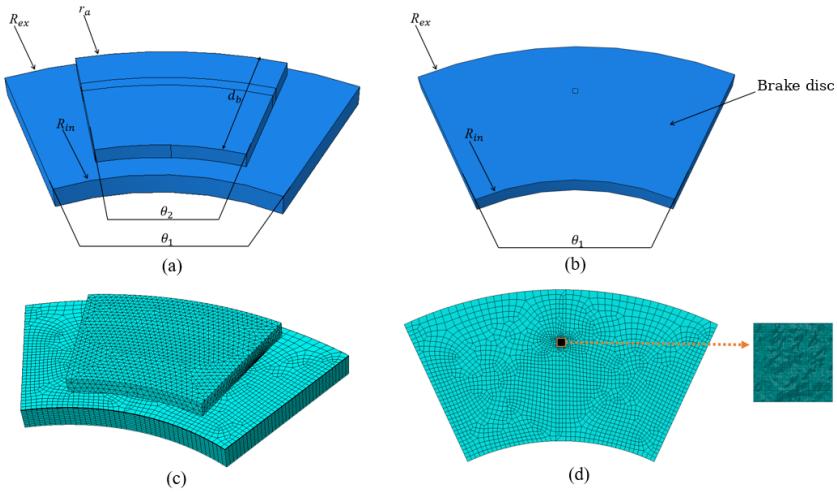

Fig 1. Model and mesh of the 5×5×1 mm³ single-sided rough brake friction pair

2.2. Thermo-Mechanical Coupling Equations and Material Model

A transient coupled temperature-displacement solution is adopted. Both the initial and ambient temperatures are 25 °C, the friction coefficient is 0.4, and the analysis duration is 200 μs. The temperature variation in the rough body is governed jointly by heat conduction, interfacial frictional heat, plastic-dissipation heat, and the thermoelastic coupling term [4,6,10]:

$$\rho C_V \frac{\partial T}{\partial t} = k\nabla^2 T + \beta\boldsymbol{\sigma} : \dot{\boldsymbol{\varepsilon}}^p - \boldsymbol{D} : \alpha \boldsymbol{I} : \left(\dot{\boldsymbol{\varepsilon}} - \dot{\boldsymbol{\varepsilon}}^p\right) T + \mu pv \tag{2}$$

where ρ, C_v, and k are the density, specific heat capacity, and thermal conductivity, respectively; β is the Taylor-Quinney coefficient; σ is the stress tensor; ε^p is the plastic strain rate; α is the coefficient of thermal expansion; and D is the elastic tensor. Interfacial heat mainly controls surface temperature rise, the plastic term describes irreversible volumetric heat generation, and the thermoelastic term represents transient exchange between recoverable strain energy and thermal energy.

Material yielding is described using the von Mises criterion and the J_2 flow rule. In the plastic stage, the Johnson-Cook model is used to characterize strain hardening, strain-rate effects, and thermal softening [8]:

$$\sigma_f = \left[A + B\left(\bar{\varepsilon}^{pl}\right)^n\right]\left[1 + C\ln\left(\frac{\dot{\bar{\varepsilon}}^{pl}}{\dot{\varepsilon}_0}\right)\right]\left[1 - \left(T^*\right)^m\right] \tag{3}$$

$$\bar{\varepsilon}_f^{pl} = \left[d_1 + d_2\exp\left(d_3\eta\right)\right]\left[1 + d_4\ln\frac{\dot{\bar{\boldsymbol{\varepsilon}}}^{pl}}{\dot{\boldsymbol{\varepsilon}}_0}\right]\left[1 + d_5\left(T^*\right)\right] \tag{4}$$

To describe both thermal risk and dynamic risk, the volumetric power density of each element is integrated into total power and normalized by the nominal contact area to obtain the thermoelastic power fraction η_{elast} and the plastic power fraction η_{plast}. In addition, the relative oscillation amplitude A_{rel}, root-mean-square amplitude A_{rms}, dominant frequency, and total oscillation energy are used to characterize stress fluctuation. The relevant indicators are defined as:

$$A_{rel} = \frac{\sigma_{max} - \sigma_{min}}{\bar{\sigma}} \times 100\% \tag{5}$$

$$A_{rms} = \sqrt{\frac{1}{N}\sum_{n=1}^{N}(\sigma[n] - \bar{\sigma})^2} \tag{6}$$

$$f_{dominant} = \underset{f \in [f_{\min}, f_{\max}]}{argmax}[PSD(f)] \tag{7}$$

$$E_{total} = \sum_{k=0}^{N/2} PSD[k] \cdot \Delta f \tag{8}$$

$$P_{input} = \frac{\mu pv}{A_{break}} \tag{9}$$

$$\eta_{plast} = \frac{\sum_{i=1}^{N}\left[\left(\boldsymbol{D} : \alpha\boldsymbol{I} : \left(\dot{\boldsymbol{\varepsilon}} - \dot{\boldsymbol{\varepsilon}}^p\right)T\right)_i dV_i\right]}{P_{input} \times A_{nominal}} \times 100\% \tag{10}$$

$$\eta_{elast} = \frac{\sum_{i=1}^{N}\left[\left(\beta\boldsymbol{\sigma}:\dot{\boldsymbol{\varepsilon}}^{p}\right)_{i} dV_{i}\right]}{P_{input}\times A_{nominal}}\times 100\% \tag{11}$$

Here, the thermoelastic power can be positive or negative, reflecting reversible thermal-mechanical energy exchange, whereas the plastic power is generally positive and represents irreversible dissipation. The frequency-domain indicators are obtained from the fast Fourier transform of the von Mises equivalent stress time series.

2.3. Operating Conditions

The finite element calculations are performed in Abaqus/Explicit. The main body of the brake disc uses C3D8T thermally coupled hexahedral elements, while thermally coupled tetrahedral elements are used in geometrically complex regions. The minimum element size in the rough region is 40 μm, corresponding to approximately 487,900 local elements. The brake disc material is Q345B, and the brake pad is a copper-based powder metallurgy material. After mesh refinement to 40 μm, the elastoplastic dissipation depth curve is essentially converged, with a maximum relative error of approximately 4.18%.

Three comparative operating conditions are defined: Case 1 is 12 kN and 48 rad/s; Case 2 is 16 kN and 48 rad/s, used to identify the load effect; and Case 3 is 16 kN and 42 rad/s, compared with Case 2 to identify the rotational-speed effect. The angular speeds of 48 rad/s and 42 rad/s correspond to linear speeds of approximately 14.16 m/s and 12.39 m/s in the rough region. In the risk discrimination framework, peak temperature and thermal affected depth represent thermal concentration, while root-mean-square stress amplitude and relative amplitude represent the fluctuation intensity caused by contact reconstruction.

Table 1. Three operating conditions

Case	Normal load/kN	Back pressure on pad/MPa	Rotational speed/(rad·s^{-1})
1	12	0.636619	48
2	16	0.848826	48
3	16	0.848826	42

3. RESULTS AND DISCUSSION

3.1. Surface Temperature Response and Load-Speed Differences

Under all three operating conditions, the high-temperature regions appear as discrete patches formed by load-bearing asperities, and they undergo initiation, expansion, and local coalescence during sliding. At the same rotational speed of 48 rad/s, increasing the load from 12 kN to 16 kN raises the maximum temperature from 957.03 °C to 993.10 °C, corresponding to an increase of 3.77%. Although the temperature peak changes only moderately, the hot-spot area and persistence both increase, indicating that load mainly strengthens local heat sources by increasing the real contact pressure and the number of asperities participating in load bearing.

When the rotational speed is reduced to 42 rad/s under 16 kN, the maximum temperature decreases to 709.20 °C, which is 28.59% lower than that under the high-load high-speed condition. This result shows that rotational speed is more sensitive to the frictional work input per unit time and to early-stage heat accumulation. It should be noted that the decrease in temperature only reflects weakened

heat input and does not directly indicate that the contact network has become stable; the stress field and frequency-domain fluctuations must also be evaluated.

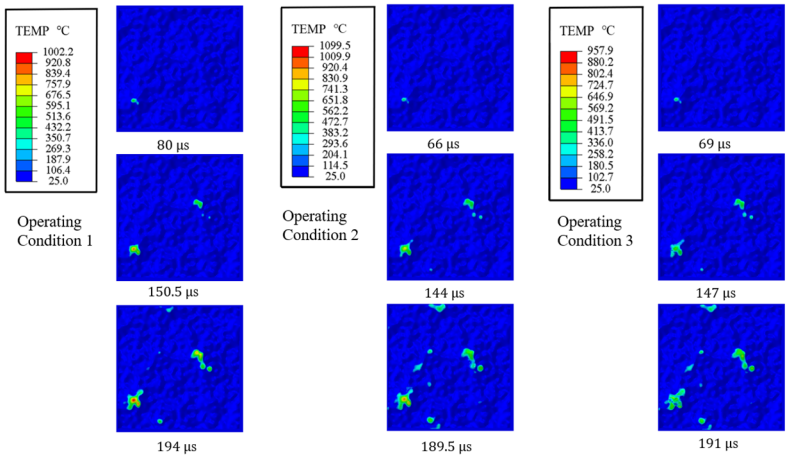

Fig 2. Evolution of the surface temperature field in the 5×5×1 mm³ rough region under three operating conditions

3.2. Stress-Field Redistribution and Spatial Mismatch

High-stress regions are mainly distributed at the edges and roots of load-bearing asperities and around hot spots. The peak stresses in Cases 1 and 2 are 986.1 MPa and 997.9 MPa, respectively, an increase of only 1.20%. However, the connected range and duration of the high-stress regions increase markedly. This indicates that the risk associated with normal load is reflected not only in the single-point peak value but also in more frequent load transfer between adjacent contact spots.

In Case 3, the peak stress decreases to 921.2 MPa, but the stress curve still exhibits pronounced fluctuations in the later stage. Temperature hot spots and high-stress regions do not completely coincide: temperature is governed by the accumulation and diffusion of frictional work, whereas stress also depends on asperity geometry, root constraints, thermal softening, and contact-spot migration. Therefore, a single temperature map cannot replace an assessment of the stability of the load-bearing network.

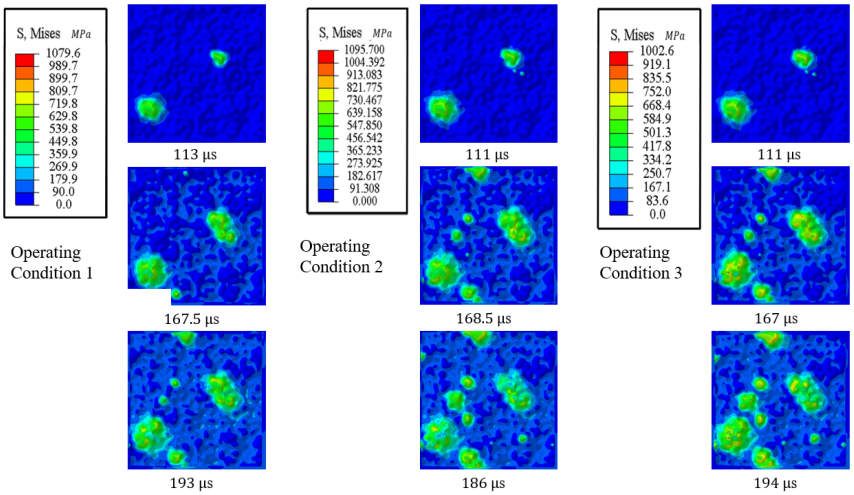

Fig 3. Evolution of the von Mises equivalent stress field in the 5×5×1 mm³ rough region under three operating conditions

Table 2. Main thermo-mechanical responses of the 5×5×1 mm³ model

Case	Maximum temperature/°C	Peak stress/MPa	Thermal affected depth/mm	Thermoelastic depth/mm	Plastic-dissipation depth/mm
1	957.03	986.1	0.497	1.296	0.204
2	993.1	997.9	0.440	1.291	0.300
3	709.2	921.2	0.366	1.290	0.301

3.3. Heat Diffusion and Elastoplastic Affected Layers

The temperature extracted along the normal direction from the highest contact point shows that the temperature reaches its peak at the surface and decays rapidly within 0.1 mm. The thermal affected depths in Cases 1, 2, and 3 are 0.497, 0.440, and 0.366 mm, respectively. After the load is increased, the heat source becomes more surface-localized; after the rotational speed is reduced, the amount of heat that can propagate into the depth within 200 μs decreases further.

The thermoelastic effect can propagate to approximately 1.29 mm, and the differences among the three operating conditions are very small, indicating that recoverable thermal-stress disturbances are mainly controlled by material properties and geometric constraints. Plastic dissipation is concentrated in the near-surface layer and is strongly affected by load: when the load increases from 12 kN to 16 kN, its affected depth increases from 0.204 mm to 0.300 mm, an increase of 47.06%; after reducing the rotational speed under 16 kN, the depth remains 0.301 mm. Thus, reducing the rotational speed can weaken heat diffusion, but it is difficult to shrink the plastic damage layer formed under high load.

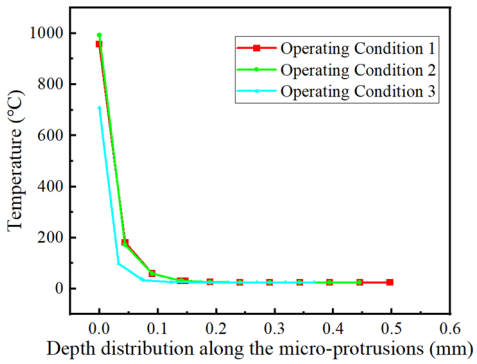

Fig 4. Temperature attenuation along the depth direction in the 5×5×1 mm³ model under three operating conditions

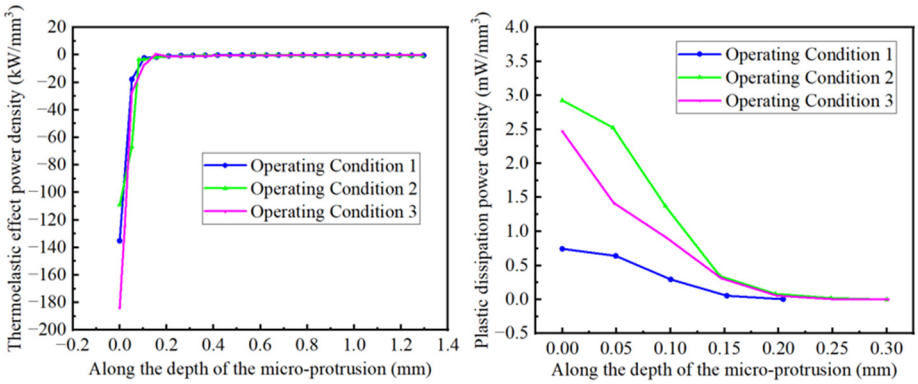

Fig 5. Depth distributions of thermoelastic effect and plastic-dissipation power in the 5×5×1 mm³ model under three operating conditions

3.4. Sequence of Thermo-Mechanical Responses

All three operating conditions exhibit a sequence in which stress is established first and temperature accumulates afterward. At the initial loading stage, the normal pressure and tangential friction force first concentrate on a small number of asperities, causing stress to rise rapidly. Subsequently, continuous frictional heat input induces thermal expansion, thermal softening, and migration of load-bearing points, after which stress drops from its peak and enters a fluctuating stage. Local thermal instability is therefore not a purely heat-transfer process, but the result of the combined action of mechanical loading rate, frictional heat generation rate, and material softening.

The temperature-rise rate and final temperature in Case 2 are both higher than those in Case 1, reflecting the strengthening effect of high load on local heat sources. In Case 3, the temperature decreases significantly, but the later-stage stress fluctuation becomes stronger, indicating that speed reduction weakens the heat input rate rather than the repeated reconstruction mechanism of contact spots under high load.

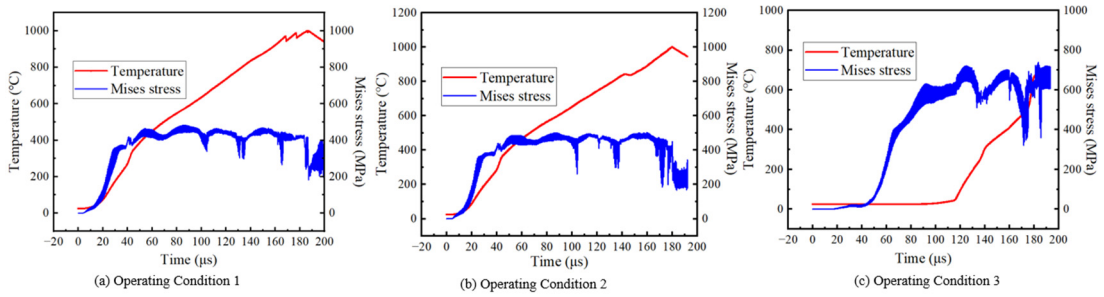

Fig 6. Time-domain evolution of temperature and von Mises equivalent stress in the 5×5×1 mm³ model under three operating conditions

3.5. Separation Between Dominant Mode and Fluctuation Intensity

Power spectral analysis shows that the dominant frequencies of the three operating conditions are 1243.01, 1297.86, and 1291.16 Hz, respectively, with a maximum difference of only 4.41%. This indicates that the main oscillation mode of the 5 mm computational domain is relatively stable. After the load increases, the dominant frequency shifts slightly toward higher frequency, which can be interpreted as an increase in contact stiffness and load-switching rhythm.

Similar dominant frequencies do not imply the same degree of instability. The root-mean-square stress amplitudes in Cases 1, 2, and 3 are 128.98, 137.84, and 265.79 MPa, respectively, and the relative amplitudes are 133.21%, 130.52%, and 182.44%, respectively. Although the high-load lower-speed condition has the lowest temperature, it exhibits the strongest stress fluctuation, indicating that the interface may display either high-temperature-concentration instability or high-fluctuation instability. Evaluation should therefore not be based only on maximum temperature.

Table 3. Stress oscillation characteristic parameters of the 5×5×1 mm³ model

Case	Mean stress/MPa	Relative amplitude/%	RMS amplitude/MPa	Dominant frequency/Hz	Total oscillation energy/(MPa)²
1	362.09	133.21	128.98	1243.01	12907.33
2	384.19	130.52	137.84	1297.86	15291.43
3	404.93	182.44	265.79	1291.16	15085.97

3.6. Reversible and Irreversible Energy Pathways

The thermoelastic power fraction alternates between positive and negative values around zero. A positive value indicates that elastic strain energy is released into heat, whereas a negative value indicates that part of the heat is temporarily converted into mechanical energy, reflecting reversible exchange during asperity contact. The plastic power fraction is generally positive and increases as contact is established, representing irreversible deformation and its associated dissipation.

The plastic-power responses in Cases 2 and 3 are both higher than that in Case 1, further indicating that plastic dissipation is mainly controlled by normal load. Reducing the rotational speed mainly changes the timing and fluctuation rhythm of the power response, but does not alter the coexistence of the thermoelastic and plastic energy pathways.

Because the 5 mm region contains many load-bearing points, the input energy can be dispersed within the contact network, and the power-fraction curves are relatively smooth. This smoothness reflects a statistically stable state in which multiple asperities work together, rather than the disappearance of local thermo-mechanical responses.

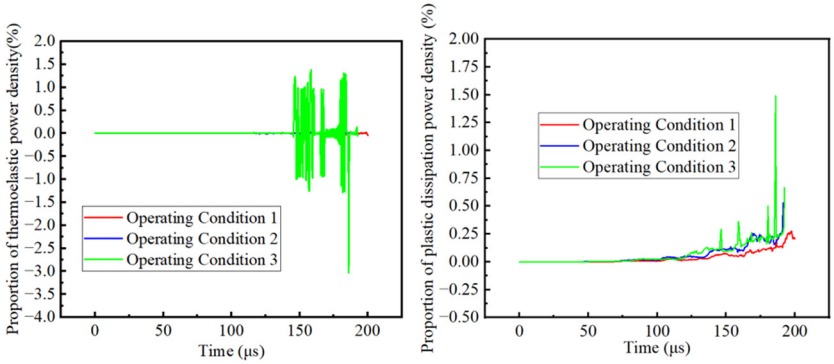

Fig 7. Thermoelastic and plastic power fractions in the 5×5×1 mm³ model under three operating conditions

3.7. Risk Discrimination Under Load-Speed Decoupling

By integrating peak temperature and stress amplitude, the three operating conditions can be placed within a two-dimensional risk framework. The high-load high-speed condition has the highest temperature and relatively high plastic-dissipation intensity, and can be classified as a high-temperature-concentration type. The high-load lower-speed condition shows a decrease in temperature but a significant increase in root-mean-square stress amplitude, and can be classified as a high-fluctuation type. The low-load high-speed condition has relatively low values for both types of indicators and can serve as the reference state. This classification shows that reducing speed mainly lowers thermal risk, whereas reducing load is more favorable for suppressing contact reconstruction and plastic-zone expansion.

In engineering evaluation, peak temperature or thermal affected depth can be used as thermal-concentration indicators, while root-mean-square stress amplitude or relative amplitude can be used as dynamic indicators. Only when both types of indicators decrease simultaneously can the interface stability be considered to have improved substantially. If temperature decreases while fluctuation increases, risk still needs to be reduced by optimizing the distribution of normal load, improving contact uniformity, or enhancing the high-temperature load-bearing capacity of the material.

3.8. Applicability Boundaries and Limitations of the Model

The conclusions of this study are based on a 5×5×1 mm³ single-sided rough computational domain, a given fractal topography, and three groups of load-speed operating conditions. This region contains 496 asperities, which can reduce random jumps caused by individual asperity geometry and is suitable for comparing operating-condition mechanisms. However, its role is to provide stable local computational results, and it is not equivalent to long-duration temperature-rise prediction for the entire disc.

The model adopts a single-sided roughness equivalence, a constant friction coefficient, and specified material parameters. It does not explicitly consider the pairing of two rough surfaces, topographic evolution caused by wear, variation of the friction coefficient with temperature, or high-temperature phase transformation of the material. Therefore, the peak temperatures reported in this paper are more suitable for relative comparison among operating conditions and should not be used directly as universal failure thresholds for all braking systems.

The calculation duration is 200 μs, which mainly captures early-stage flash temperature, plastic dissipation, and stress oscillation after micro-contact establishment. Actual braking also involves second-scale global heat accumulation, convective and radiative heat dissipation, and macroscopic structural thermal deformation. In future work, the local roughness model should be coupled with a full-disc thermal boundary model.

In addition, the dual-risk discrimination method is currently verified using only three representative operating conditions. Future studies should expand the load and speed parameter space and combine infrared thermometry, vibration signals, or acoustic emission signals to experimentally validate the correspondence between temperature concentration and stress fluctuation.

4. CONCLUSION

(1) The 5×5×1 mm³ rough computational domain can stably reproduce discrete hot spots formed by multiple asperities, network-like stress transfer, and separable thermoelastic-plastic affected layers, making it suitable for comparing the effects of load and rotational speed on local thermal instability.

(2) At the same rotational speed of 48 rad/s, increasing the load from 12 kN to 16 kN raises the maximum temperature from 957.03 °C to 993.10 °C, and increases the plastic-dissipation depth from 0.204 mm to 0.300 mm. Load mainly strengthens the load-bearing network, plastic-zone expansion, and local heat-source concentration.

(3) Under 16 kN, reducing the rotational speed from 48 rad/s to 42 rad/s lowers the maximum temperature to 709.20 °C, but increases the root-mean-square stress amplitude to 265.79 MPa. Reducing rotational speed can weaken early-stage heat accumulation, but it cannot eliminate high-load-driven contact reconstruction and stress fluctuation.

(4) The stability of rough braking interfaces should be evaluated jointly using the two indicators of temperature concentration and stress fluctuation. The high-load high-speed condition tends toward high-temperature-concentration risk, whereas the high-load lower-speed condition tends toward high-fluctuation risk. Controlling the concentration of normal load is more effective than simply reducing speed for decreasing both types of risk simultaneously.

REFERENCES

[1] Greenwood, J. A., & Williamson, J. B. P. (1966). Contact of nominally flat surfaces. *Proceedings of the Royal Society of London. Series A. Mathematical and Physical Sciences*, 295(1442), 300–319. https://doi.org/10. 1098/ rspa.1966.0242.

[2] Blok, H. (1963). The flash temperature concept. *Wear*, 6(6), 483–494. https://doi.org/10.1016/0043-1648(63)90038-1.

[3] Bowden, F. P., & Tabor, D. (2001). *The friction and lubrication of solids*. Oxford University Press.

[4] Barber, J. R. (1969). Thermoelastic instabilities in the sliding of conforming solids. *Proceedings of the Royal Society of London A: Mathematical and Physical Sciences*, 312(1510), 381–394. https://doi.org/10.1098/rspa.1969.0161.

[5] Zagrodzki, P. (2009). Thermoelastic instability in friction clutches and brakes: Transient modal analysis. *International Journal of Solids and Structures*, 46(11–12), 2463–2476. https://doi.org/10.1016/j.ijsolstr.2009.01.010.

[6] Jaeger, J. C. (1942). Moving sources of heat and the temperature at sliding contacts. *Journal and Proceedings of the Royal Society of New South Wales*, 76(3), 203–224.

[7] Sofuoglu, H., & Ozer, A. (2008). Thermomechanical analysis of elastoplastic medium in sliding contact with fractal surface. *Tribology International*, 41(8), 783–796. https://doi.org/10.1016/j.triboint.2007.12.003.

[8] Johnson, G. R., & Cook, W. H. (1983). A constitutive model and data for metals subjected to large strains, high strain rates and high temperatures. In *Proceedings of the 7th International Symposium on Ballistics* (pp. 541–547). International Ballistics Committee.

[9] Meng, D., Li, B., Zhang, L., et al. (2024). Research on the evolution of friction hot spots in vehicle disc brake during braking based on experiment. *International Journal of Thermal Sciences*, 203, 109126. https://doi.org/10. 1016/j. ijthermalsci. 2024.109126.

[10] Waddad, Y., Magnier, V., Dufrenoy, P., et al. (2019). Heat partition and surface temperature in sliding contact systems of rough surfaces. *International Journal of Heat and Mass Transfer*, 137, 1167–1182. https://doi. org/ 10. 1016/ j.ijheatmasstransfer.2019.03.120.